PAPER

Spatially resolved stoichiometry determination of Li₇La₃Zr₂O₁₂ solid-state electrolytes using LA-ICP-OES

Stefan Smetaczek, [ID] [a] Maximilian Bonta,[a] Andreas Wachter-Welzl,[a] Stefanie Taibl, [ID] [a] Reinhard Wagner,[b] Daniel Rettenwander, [ID] [c] Jürgen Fleig [ID] [a] and Andreas Limbeck [ID] *[a]

Cubic Li₇La₃Zr₂O₁₂ (LLZO) garnets are among the most promising solid-state electrolytes for next-generation Li batteries. However, despite intensive research in recent years, little effort is spent on proper chemical analysis of the material. For reliable LLZO investigation, knowledge about the exact chemical composition, especially the Li content, is of uttermost importance. Herein, we present a method for the laterally resolved stoichiometry determination of Al stabilized LLZO ($Li_{7-3x}Al_xLa_3Zr_2O_{12}$) using LA-ICP-OES. To ensure reliable signal quantification, matrix-matched standards are prepared and carefully characterized using sample digestion and liquid ICP-OES measurement. An internal standard-independent calibration strategy based on 100 m% normalization is applied, enabling the quantification of all cations within the material. By comparing the obtained high-precision LA-ICP-OES calibrations with analog LA-ICP-MS measurements, it is shown that ICP-OES is the superior choice for the analysis of Li. The developed method is applied to record quantitative distribution images of an Al stabilized LLZO pellet, revealing macroscopic stoichiometry variations within the sample. To verify the analysis, the average stoichiometry obtained by the LA measurements is compared with the bulk composition determined *via* liquid ICP-OES analysis after sample fusion. The obtained values show excellent agreement, confirming the accuracy of the developed method.

1. Introduction

Due to the rapid development of portable electronic devices as well as the growing electric car industry, more and more powerful batteries are needed. Among all known batteries, Li-based ones offer the highest volumetric and gravimetric energy density and are therefore the most promising option to face the upcoming challenges.[1] However, most rechargeable Li-ion batteries currently in use employ electrolytes composed of organic solvents or polymers with a dissolved Li-salt.[2] Since these feature many unwanted properties such as flammability, poor electrochemical stability and a limited temperature range of operation, it is of major interest to replace them by more stable inorganic solid electrolytes.[3]

A variety of inorganic solid Li-ion conductors have been considered for use in all-solid state batteries.[3–6] While some of the proposed solid electrolytes exhibit Li-ion conductivity comparable to organic liquid electrolytes, the performance of

batteries based on these inorganic ion conductors is still inferior to that of commercially available Li-ion batteries.[6] Several key challenges remain, such as poor electrolyte/electrode interface, instability in ambient environment, flexibility concerns, and poor cycling stability.[6–9] One of the most promising solid electrolytes is the Li stuffed garnet Li₇La₃Zr₂O₁₂ (LLZO), which was first reported by Murugan *et al.* in 2007.[10] Beside its high Li-ion conductivity (up to 10^{-3} S cm^{-1} at ambient temperature) and high electrochemical stability window, it also features chemical stability against elemental Li, which enables the use in Li-metal batteries.[10–13]

Pure LLZO crystalizes in two different polymorphs: a tetragonal and a cubic modification. For use as a Li-ion conductor, the cubic structure is much more desirable since its Li-ion conductivity is two orders of magnitude higher compared to the tetragonal variant.[14,15] The highly conductive cubic modification is not stable at room temperature, however, stabilization is achieved by partial Al-substitution (3 Li$^+$ → Al^{3+}), resulting in the formula unit $Li_{7-3x}Al_xLa_3Zr_2O_{12}$.[16–18]

Although a lot of research has been focused on LLZO in recent years, the reproducible synthesis of garnets with high Li-ion conductivity remains challenging. For example, pellets with the same nominal composition prepared at different laboratories show differences in ionic conductivity of more than an

[a]Institute of Chemical Technologies and Analytics, TU Wien, Vienna, Austria. E-mail: Andreas.Limbeck@tuwien.ac.at

[b]Department of Chemistry and Physics of Materials, University Salzburg, Salzburg, Austria

[c]Institute for Chemistry and Technology of Materials, TU Graz, Graz, Austria

order of magnitude.[11,19] Furthermore, local conductivity variations have been reported within one and the same sample.[20] The reasons for these variations are still not completely understood, however, they probably relate to differences in sample stoichiometry.[19] Since synthesis of LLZO normally involves high-temperature treatment, partial loss of Li_2O due to evaporation cannot be avoided.[21,22] In addition, Al incorporation from the commonly used Al_2O_3 crucibles further changes the sample composition.[16,17,21] Thus, determination of the chemical composition after the synthesis is crucial for reliable LLZO investigation.

Chemical analysis of Al-stabilized LLZO pellets is mostly performed using sample-digestion and subsequent ICP-OES (Inductively Coupled Plasma-Optical Emission Spectroscopy) or ICP-MS (Inductively Coupled Plasma-Mass Spectrometry) analysis.[14,17,22–24] While this approach enables reliable determination of the bulk composition, it requires time consuming sample preparation and does not provide any spatially resolved information. For elemental surface analysis of LLZO, mostly EDX (Energy-Dispersive X-ray Spectroscopy) is used.[14,16,21,25,26] This method enables the determination of the Al, La, and Zr distribution, but its use is strongly limited by its incapacity to detect Li. Other applied surface analysis techniques are X-ray photoelectron spectroscopy (XPS)[27–31] and secondary ion mass spectrometry (SIMS),[32–35] however, both techniques usually only provide semi-quantitative information and are limited in terms of sampling depth (*i.e.*, surface effects and not bulk properties are investigated). Additionally, the excellent spatial resolution of SIMS with spot sizes down to the sub-µm range makes the analysis of macroscopic areas very time-consuming.

Also LIBS (Laser Induced Breakdown Spectroscopy) has been used for the elemental analysis of LLZO. Depth profiles,[36] 2D cross-sectional maps[21,27,37] and even 3D distribution images[38] have been recorded, showing that LIBS is a very powerful tool for the investigation of sample inhomogeneity close to the sample surface. In these experiments, the bulk composition of the samples (determined by ICP-OES) served as standard for signal quantification, assuming that the chemical composition is constant over the whole sample after reaching a specific sampling depth. Since one of our previous studies revealed macroscopic inhomogeneities in Al stabilized LLZO pellets,[19] this assumption does not seem to be correct for all samples, questioning the suitability of this quantification approach. Overall, there is still need for a laterally resolved method for LLZO analysis that provides reliable quantitative information.

A promising option for the chemical analysis of LLZO is coupling of ICP-MS or ICP-OES to LA (laser ablation). While the use of LA prevents time-consuming sample digestion and dilution, the subsequent analysis of the generated aerosol with ICP-OES or ICP-MS allows detection of all LLZO constituents including Li. Furthermore, these methods provide spatially resolved information and have already been used for the quantitative determination of bulk, trace and ultra-trace elements in various advanced materials including ceramics.[39,40] While neither LA-ICP-MS nor LA-ICP-OES is widely adapted in the field of Li-ion batteries, both techniques have

been successfully applied for the characterization of electrode materials.[41–45]

Since LA suffers from sample-dependent ablation behavior and elemental fractionation, reliable signal quantification is challenging. However, these issues can be overcome by using matrix-matched calibration standards in combination with appropriate signal normalization strategies.[46]

The aim of this study is to develop a method for the laterally resolved analysis of Al-stabilized LLZO ($Li_{7-3x}Al_xLa_3Zr_2O_{12}$) by using LA-ICP-OES. To ensure reliable signal quantification, we prepared matrix-matched standards and characterized them by sample digestion and subsequent liquid ICP-OES measurement. We used these standards to obtain LA-ICP-OES calibrations, and compared the results with parallel LA-ICP-MS measurements. To show the capabilities of the developed method, we recorded quantitative distribution images of an Al stabilized LLZO pellet.

2. Experimental

2.1 LLZO synthesis

$Li_{7-3x}Al_xLa_3Zr_2O_{12}$ garnets with intended Al contents ranging from $x = 0.00$ to $x = 0.40$ were synthesized using a high-temperature sintering route based on the procedure described by Wagner *et al.*[47] Li_2CO_3 (≥99%, Merck, Germany), Al_2O_3 (≥99.5%, Sigma-Aldrich, Germany), La_2O_3 (≥99.99%, Carl Roth, Germany), and ZrO_2 (≥99%, Carl Roth, Germany) were used as starting materials. The reagents were weighed in the intended stoichiometric proportions with an excess of 10 m% Li_2CO_3 to compensate Li_2O loss during sintering. The powders were ground and mixed in an agate mortar under addition of isopropyl alcohol and subsequently cold-pressed into pellets using a uniaxial press. The resulting pellets were put into an alumina crucible and placed on a pellet of pure LLZO to avoid undesired Al contamination from the crucible. The samples were heated to 850 °C with a rate of 5 °C min^{-1} and calcined for 4 h. After cooling down, the resulting pellets were again ground in an agate mortar and ball-milled for 1 h under isopropyl alcohol (FRITSCH Pulverisette 7, Germany, 800 rpm, 2 mm ZrO_2 balls). After drying, the powders were cold-pressed, and the resulting pellets were again put into an alumina crucible. The samples were placed between two pellets of pure LLZO to avoid unwanted incorporation of Al^{3+} from the crucible as well as formation of extra phases due to loss of Li_2O during the final sintering step. The pellets were sintered for 6 h at 1230 °C in a muffle furnace using air atmosphere and a heating rate of 5 °C min^{-1}.

2.2 Preparation of matrix-matched standards

A series of $Li_{7-3x}Al_xLa_3Zr_2O_{12}$ standards was prepared from synthesized LLZO pellets with intended Al contents of $x = 0.00$, 0.05, 0.10, 0.15, 0.20, 0.25, 0.30, 0.35, 0.40. To ensure homogeneity, we crushed and ground the pellets in an agate mortar. We then transferred about 1 g of each of the obtained powders into a flexible silicone rubber mold and cold pressed them using a mechanical isostatic press (Paul-Otto Weber, Germany) at a pressure of 300 MPa. To remove potential surface

This journal is © The Royal Society of Chemistry 2020

J. Anal. At. Spectrom., 2020, **35**, 972–983 | **973**

contaminations caused by the pressing mold, we cleaned the sample surface using P2000 SiC grinding paper (Struers, Denmark). The procedure resulted in pressed pellets with about 8 mm diameter and about 5 mm thickness.

2.3 Bulk analysis *via* liquid ICP-OES

The prepared LLZO standards were characterized using liquid ICP-OES analysis. For that purpose, we digested parts of the powders that were used to press the standard pellets. We used borax fusion for the sample digestion: The sample powders were transferred into Pt crucibles, mixed with a 16-fold excess of sodium tetraborate (anhydrous, $\geq$ 98%, Merck, Germany), and heated to 1000 °C for 5 h. We replicated the digestion three times for each standard (50 mg per replicate). Additionally, we performed blank digestions without sample to check for potential contaminations caused by the sample pretreatment. After cooling down, we dissolved the solidified fusions using a 8/1/40 (v/v/v) mixture of hydrochloric acid (37 m%, EMSURE®, Merck, Germany), hydrofluoric acid (40 m%, EMSURE®, Merck, Germany), and deionized water (18.2 MΩ cm^{-1}) obtained by Barnstead™ Easypure™ II (Thermo Fisher Scientific, USA). The prepared solutions were diluted to a final LLZO concentration of about 18 mg kg^{-1} using a 1/100 (v/v) dilution of nitric acid (65 m%, EMSURE®, Merck, Germany).

For signal quantification, univariate calibration using certified single element ICP-standard solutions (Certipur®, Merck, Germany) was used. We mixed Al, La, Li, and Zr standards to obtain elemental ratios corresponding to a $Li_{6.4}Al_{0.2}La_3Zr_2O_{12}$ sample. By diluting the standard mixture, we prepared calibration standards with an LLZO concentration ranging from 3.6 to 36 mg kg^{-1}. We added an Eu ICP-standard solution (Certipur®, Merck, Germany) to all standard and sample solutions to a final concentration of 0.2 mg kg^{-1} and used Eu as internal standard for the analysis.

An iCAP 6500 RAD (Thermo Fisher Scientific, USA) equipped with an echelle-type monochromator and a CID detector was used for the ICP-OES analysis. For data acquisition, we used Qtegra software provided by the manufacturer of the instrument. Introduction of the samples was performed using an ASX-520 autosampler (CETAC Technologies, USA), PTFE tubing, and a sample introduction kit consisting of a conventional Meinhard high-solids quartz nebulizer and a quartz cyclone spray chamber without ascension tube. We used a plasma torch containing a quartz injector tube with 1.5 mm inner diameter. Detailed information about the used instrument parameters can be found in Table 1.

For each analyte, we recorded the two most sensitive and non-interfered emission lines. Only one emission line per element was used for quantification, the other one was used for quality control (*i.e.*, check for spectral interferences). In case of Al only one emission line with sufficient signal intensity was accessible (396.152 nm). Since this line suffers from spectral interference caused by a minor Zr emission line, we applied interference correction. For that purpose, we analyzed Zr single element standard solutions with various concentrations to determine the impact of the interference.

Table 1 Instrumental settings for bulk analysis *via* ICP-OES

	Thermo iCAP 6500 RAD
RF power	1200 W
Radial observation height	12 mm
Plasma gas flow (Ar)	12 l min^{-1}
Nebulizer gas flow (Ar)	0.6 l min^{-1}
Auxiliary gas flow (Ar)	0.8 l min^{-1}
Integration time	5 s
Replicates per sample	5
Purge pump rate	1.6 ml min^{-1}
Sample flow rate	0.8 ml min^{-1}
Analytical wavelengths	
Eu (internal standard)	281.396 nm ([b]) 381.967 nm ([c])
Al	396.152 nm[a,c]
La	333.749 nm[b] 412.323 nm[a,b]
Li	610.362 nm[c] 670.784 nm[a,c]
Zr	339.198 nm[b] 343.823 nm[a,b]

[a] Used for quantification. [b] Normalized to Eu 281.396 nm signal [c] Normalized to Eu 381.967 nm signal.

For the compensation of differences in sample introduction and instrumental drifts, we used Eu as internal standard and normalized all signals to a corresponding emission line. To further minimize errors in signal quantification, we took two additional measures: (a) we measured the calibration standards not consecutively but separately between the samples and in random order and (b) we repeated the whole analysis three times. The analyte concentrations obtained this threefold analysis were averaged for further data processing.

2.4 LA-ICP-OES and -MS calibration

For all LA experiments, we utilized a NWR213 laser ablation system (ESI, USA) equipped with a frequency quintupled 213 nm Nd:YAG laser and a fast-washout ablation cell always positioned above the actual ablation site. We coupled the device to either ICP-OES or ICP-MS using PTFE tubing with 2 mm inner diameter. He was used as a carrier gas for cell washout, which was mixed with Ar make-up gas upon introduction into the plasma. Detailed information about the used instrumental settings can be found in Table 2.

For the LA-ICP-OES experiments, the same ICP-OES instrument as for the bulk analysis was used (*cf.* Section 2.3). In contrast to the liquid measurements, a plasma torch containing a corrosion-resistant ceramic injector tube was used. Data acquisition was performed using iTEVA software (v.2.8.0.96) provided by the manufacturer of the instrument. For each analyte, we recorded two emission lines, where one emission line was used for signal quantification and the other one was used for quality control. Compared to the liquid analysis, we selected less sensitive La and Zr emission lines to avoid detector saturation. Furthermore, we reduced the integration time to 1 s in order to allow fast monitoring of the transient signals provided in imaging experiments. Similar to the liquid measurements, we applied interference correction for the Al 396.152 nm emission lines. In order to determine the impact of

974 | *J. Anal. At. Spectrom.,* 2020, **35**, 972–983

This journal is © The Royal Society of Chemistry 2020

Table 2 Instrumental settings LA-ICP-OES and -MS analysis

Laser ablation system	ESI NWR213
Average fluence	
Pre-ablation	2.50 J cm^{-2}
Analysis	4.25 J cm^{-2}
Laser diameter	
Pre-ablation	250 μm
Analysis	100 μm
Scan speed	
Pre-ablation	250 μm s^{-1}
Analysis	100 μm s^{-1}
Repetition rate	20 Hz
Carrier gas flow (He)	0.6 l min^{-1}
Make-up gas flow (Ar)	0.8 l min^{-1}
ICP-OES instrumentation	Thermo iCAP 6500 RAD
RF power	1200 W
Radial observation height	12 mm
Plasma gas flow (Ar)	12 l min^{-1}
Auxiliary gas flow (Ar)	0.5 l min^{-1}
Integration time	1 s
Analytical wavelengths	
Al	309.271 nm 396.152 nm[a]
La	261.034 nm[a] 419.655 nm
Li	610.362 nm[a] 670.784 nm
Zr	257.139 nm[a] 274.256 nm
ICP-MS instrumentation	Thermo iCAP Q
RF power	1550 W
Plasma gas flow (Ar)	14 l min^{-1}
Auxiliary gas flow (Ar)	0.8 l min^{-1}
Dwell time per isotope	10 ms
Cones	Ni
Mass resolution	$m/\Delta m = 300$
Measured isotopes	^{7}Li, ^{27}Al, ^{90}Zr, ^{138}La

[a] Used for quantification.

the Zr interference, we measured an Al-free YSZ single crystal (ZrO$_2$ stabilized with 9.5 mol% Y$_2$O$_3$, 5 mm × 5 mm × 0.5 mm, Crystec, Germany) prior to the analysis using identical instrument setting.

In case of the LA-ICP-MS measurements, the LA system was coupled to a quadrupole ICP-MS instrument (Thermo iCAP Qc, ThermoFisher Scientific, Germany). For data acquisition, we used Qtegra software (v.2.10.3324.62) provided by the manufacturer of the instrument. Before every experiment, we optimized the measurement parameters concerning the MS instrumentation using NIST 612 trace metals in glass standard (National Institute of Standards and Technologies, Gaithersburg, MD) for maximum ^{115}In signal. Additionally, we monitored the oxide ratio by the ^{140}Ce^{16}O/^{140}Ce ratio, which was below 2.0% for all experiments.

LA-ICP-OES and -MS measurements were quantified using the prepared LLZO pellets as matrix-matched calibration standards. Analysis of these standards was performed using line scan ablation patterns with adjoining lines. Per standard, we placed four laser patterns (each having an area of about 0.4

mm^2) on different locations on the pellets. Each laser pattern was ablated three times. For further data processing, we calculated average values for each pattern. In order to remove potential surface contaminations (e.g. Li$_2$CO$_3$ due to air exposure[27]), we employed a pre-ablation step consisting of a similar line scan patterns prior to the analysis.

Two different calibration strategies were used for signal quantification. On the one hand, we applied conventional univariate calibration in combination with the use of La as internal standard, assuming equal La content and -distribution in all samples. Additionally, we used an internal standard-independent calibration strategy presented by Liu et al.,[48] which was adapted for LLZO samples. Based on the consideration that the sum of all metal oxides in LLZO adds up to 100 m%, this approach uses the intensities of all measured analytes expressed as the corresponding oxides (Al$_2$O$_3$, Li$_2$O, La$_2$O$_3$, ZrO$_2$) for signal normalization. The sample composition was calculated using the following eqn (1) and (2)

$$C_{sam}^i = \frac{100\,cps_{sam}^i l^i}{\sum_{k=1}^{N}\left(cps_{sam}^k l^k\right)} \tag{1}$$

$$l^i = \sum_{j=1}^{n}\left(\frac{C_{rmj}^i}{cps_{rmj}^i}\frac{C_{rmj}^i}{\sum_{j=1}^{n}C_{rmj}^i}\right) \tag{2}$$

where N = number of measured elements, n = number of reference materials used as external standard, C_{sam}^i = concentrations of analyte element i in the sample, C_{rm}^{ji} = concentrations of analyte element i in the reference material j, $cps_{sam}^i(cps_{sam}^k)$ = net count rate of element i (k) in the sample, and cps_{rm}^{ji} = net count rate of element i in the reference material j. Detailed information about this calibration strategy can be found in ref. 48.

2.5 Elemental imaging

2D distribution images of an Al stabilized LLZO pellet with the nominal composition of Li$_{6.4}$Al$_{0.2}$La$_3$Zr$_2$O$_{12}$ were recorded using LA-ICP-OES. Prior to the analysis, we reduced the thickness of the pellet to about 250 μm using P500 SiC grinding paper (Struers, Denmark). The purpose of this was twofold: first, removing the surface near region ensures that the analysis investigates the bulk of the material. Second, a reduced sample thickness decreases the impact of composition variations perpendicular to the surface, ensuring that the average composition determined by the LA measurement (which one probes the sample surface) represents the bulk value of the whole pellet.

LA-ICP-OES settings described in the previous section were used for all measurements. To create elemental maps, we used line-scan ablation patterns with adjoining lines. A laser beam diameter of 100 μm and a scan speed of 100 μm s^{-1} were used, which, taking the washout-time of the ablation cell into consideration, results in images with a lateral resolution of 100 μm. As with the measurement of the calibration standards,
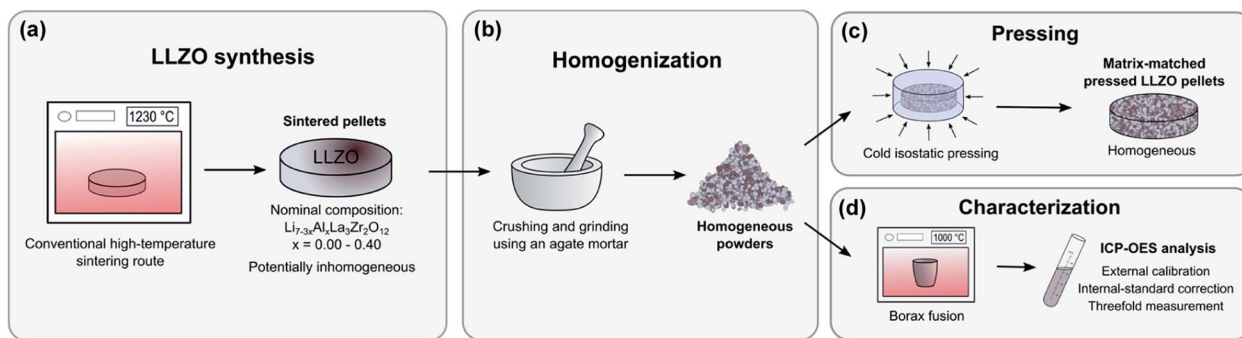
This journal is © The Royal Society of Chemistry 2020

J. Anal. At. Spectrom., 2020, **35**, 972–983 | **975**

Fig. 1 Preparation and characterization of matrix-matched LLZO standards. (a) LLZO synthesis leading to sintered pellets, followed by (b) crushing and grinding of the pellets to ensure homogeneity. The resulting powders were used for (c) pressing them into pellets to obtain homogenous standards and (d) characterizing the standards using borax fusion and ICP-OES analysis.

we also employed pre-ablation step in the sample analysis for cleaning purposes (*e.g.*, removing residues from SiC grinding paper).

Image processing was performed using the software Image-Lab (v.2.41, Epina GmbH, Austria).

2.6 Validation approach

In order to control the accuracy of the quantitative LA-ICP-OES imaging analysis, we compared the average sample stoichiometry derived from distribution maps with the bulk chemical composition determined by sample digestion and subsequent liquid ICP-OES measurement. The bulk analysis was performed after the imaging experiment using the procedure described in Section 2.3. Before the digestion, we crushed and ground the pellet (with a total mass of 30 mg) to obtain a homogeneous powder. The digestion was replicated three times, using *ca.* 10 mg sample each.

3. Results and discussion

3.1 Standard characterization

Obtaining suitable reference materials is a crucial aspect for reliable and accurate quantification of LA-ICP-OES and -MS

measurements. As for most novel materials, LLZO certified reference materials are not commercially available and in-house standard preparation is therefore necessary. Since calibration standards are a limiting factor for the accuracy of an analysis, it is important to ensure careful preparation as well as high-precision characterization of the material.

Fig. 1 shows the standard preparation and characterization process schematically. We synthesised LLZO pellets with different doping content ranging from 0.0 to 0.4 Al per formula unit (pfu) using a conventional high temperature sintering route. Since the high temperature is likely to affect the chemical composition of the pellets (*e.g.* due to loss of Li_2O or diffusion processes) leading to sample inhomogeneities, the obtained pellets are not suitable for direct use as standard. To overcome this issue, we crushed and ground the sintered pellets and subsequently pressed the obtained powders into pellets. This results in LLZO pellets with constant chemical composition that are suitable for use as matrix-matched standard in LA-ICP-OES measurements. For the characterization of the obtained standards, we used the remaining powders that were not consumed by the pressing of the standards. We transferred the samples into liquid form by using a borax fusion and analysed the obtained liquids *via* ICP-OES. To obtain results as accurate as possible, we took multiple measures: (a) three replicate digestions for each

Table 3 Chemical composition of the prepared standards (nominally $Li_{7-3x}Al_xLa_3Zr_2O_{12}$) determined *via* ICP-OES analysis. The stated measurement uncertainties correspond to the confidence intervals of the mean values derived from the measurement of three replicate digestions ($\alpha = 0.10$, $n = 3$). The nominal atomic ratios are displayed in brackets. The analysis confirms significant deviations from the intended stoichiometry, especially in case of Li

x	Al/La	Li/La	Zr/La	Formula[a]
0.00	0.025 ± 0.006 (0.000)	2.17 ± 0.04 (2.33)	0.638 ± 0.003 (0.667)	$Li_{6.51}Al_{0.08}La_3 Zr_{1.91}O_{11.7}$
0.05	0.013 ± 0.008 (0.017)	2.23 ± 0.10 (2.28)	0.651 ± 0.006 (0.667)	$Li_{6.69}Al_{0.04}La_3 Zr_{1.95}O_{11.8}$
0.10	0.029 ± 0.007 (0.033)	2.18 ± 0.03 (2.23)	0.650 ± 0.003 (0.667)	$Li_{6.55}Al_{0.09}La_3 Zr_{1.95}O_{11.8}$
0.15	0.048 ± 0.004 (0.050)	2.17 ± 0.04 (2.18)	0.653 ± 0.005 (0.667)	$Li_{6.52}Al_{0.15}La_3 Zr_{1.96}O_{11.9}$
0.20	0.066 ± 0.004 (0.067)	2.14 ± 0.06 (2.13)	0.652 ± 0.004 (0.667)	$Li_{6.42}Al_{0.20}La_3 Zr_{1.96}O_{11.9}$
0.25	0.083 ± 0.003 (0.083)	2.10 ± 0.06 (2.08)	0.651 ± 0.005 (0.667)	$Li_{6.29}Al_{0.25}La_3 Zr_{1.95}O_{11.9}$
0.30	0.097 ± 0.004 (0.100)	2.06 ± 0.06 (2.03)	0.646 ± 0.003 (0.667)	$Li_{6.19}Al_{0.29}La_3 Zr_{1.94}O_{11.9}$
0.35	0.116 ± 0.008 (0.117)	2.02 ± 0.05 (1.98)	0.653 ± 0.003 (0.667)	$Li_{6.07}Al_{0.35}La_3 Zr_{1.96}O_{12.0}$
0.40	0.137 ± 0.006 (0.133)	2.00 ± 0.03 (1.93)	0.655 ± 0.004 (0.667)	$Li_{6.00}Al_{0.41}La_3 Zr_{1.96}O_{11.9}$

[a] Calculated, based on atomic ratios. Oxygen contents are estimated from charge balance considerations.

976 | *J. Anal. At. Spectrom.*, 2020, **35**, 972–983

This journal is © The Royal Society of Chemistry 2020
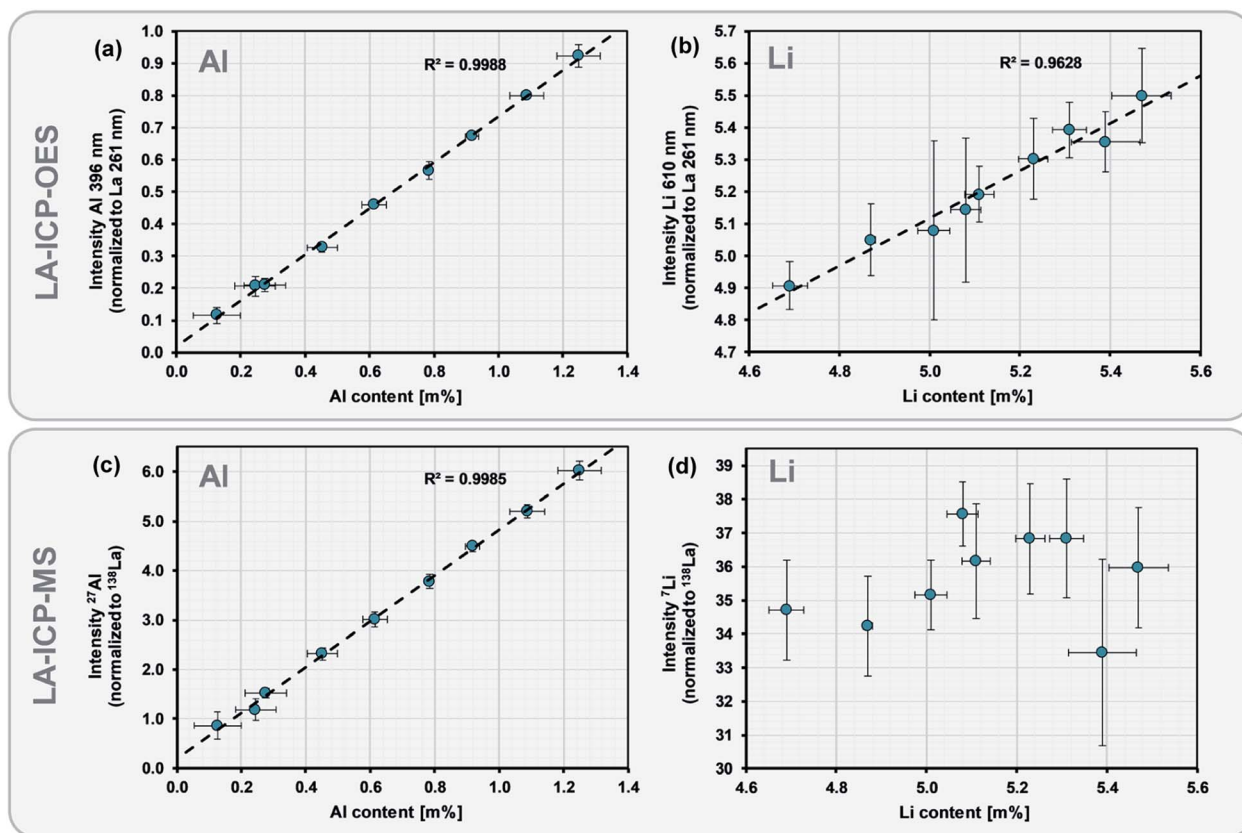
Fig. 2 LA-ICP-OES calibration of the Al (a) and Li (b) signal as well as analog LA-ICP-MS measurements (c and d). A conventional univariate calibration strategy is applied, where La is used as internal standard for signal normalization. The vertical error bars represent the confidence intervals of the mean values derived from the measurement of multiple ablation patterns ($\alpha = 0.10$, $n = 4$); the horizontal error bars represent the confidence intervals of the standard characterization via liquid ICP-OES ($\alpha = 0.10$, $n = 3$). The plots confirm LA-ICP-OES is superior to LA-ICP-MS for the determination of Li, while similar results are obtained for the analysis of Al.
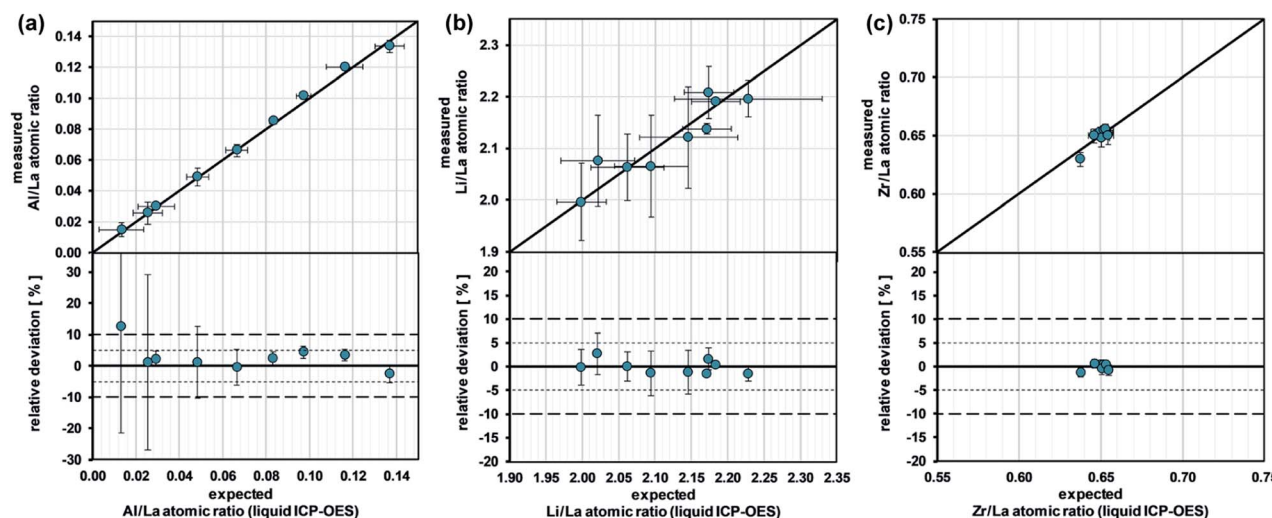

Fig. 3 Cross-validation of a LA-ICP-OES calibration using 100 m% normalization. Predicted (a) Al/La, (b) Li/La, and (c) Zr/La atomic ratios for each standard vs. corresponding target values (determined via liquid ICP-OES). In addition, the relative deviations are shown for a better visualization of the differences. The vertical error bars represent the confidence intervals of the mean values derived from the measurement of multiple ablation patterns ($\alpha = 0.10$, $n = 4$); the horizontal error bars represent the confidence intervals of the standard characterization via liquid ICP-OES ($\alpha = 0.10$, $n = 3$). The plots show an excellent agreement with a relative deviation below 5% for all Li/La and Zr/La as well as most Al/La ratios.

This journal is © The Royal Society of Chemistry 2020

J. Anal. At. Spectrom., 2020, **35**, 972–983 | **977**

sample, (b) internal-standard corrections using Eu, (c) random measuring sequence of standards and samples, (d) threefold repeat of the whole measurement including calibration, and (e) interference correction for the main Al emission line (396.152 nm, interfered by a minor Zr line). Although the Zr interference is rather weak and might not be relevant for samples with high doping contents, we still consider it necessary to prevent inaccurate results for samples with low Al concentration.

The determined bulk compositions of all standards are listed in Table 3. The results show significant but reasonable deviations from the intended values. The average Zr/La atomic ratio is 0.650, which is close to the expected value (0.667). Also the Al/La atomic ratios agree well with the intended ratios, except for the nominally Al-free standard. In this case, the standard shows a much higher Al/La ratio of 0.025, which indicates Al incorporation during the sintering in the Al_2O_3 crucibles. The reason that this can only be observed for the nominally Al-free sample could be related to the fact that Al-substitution stabilizes the cubic LLZO modification.[16–18] The strongest deviations from the intended values are observed for the Li/La atomic ratio. This is not surprising, since it is known that Li_2O evaporates during sintering, changing the Li content of the pellet. While usually Li excess is used in the starting material mixture to compensate this phenomenon,[10,16,17,49] the assumed amount of lost Li might not be correct. Interestingly, the Li/La ratio is lower than desired for the standards with low Al contents, and higher than intended for the Al-rich standards. This means that less Li was lost during the synthesis of samples with a higher Al content, indicating that the Li_2O loss depends on the Al content. Overall, the results highlight the importance of monitoring the chemical composition of LLZO samples after high-temperature treatment, not only if they are used as standards, but also for general purposes.

3.3 LA-ICP-OES calibration

After the preparation and characterization of matrix-matched LLZO standards, we used them for the calibration of the LA-ICP-OES experiments. For this purpose, we analyzed each of the pellets using multiple ablation patterns.

Fig. 2 shows typical calibrations obtained by such an experiment. Conventional univariate calibrations are displayed where signal normalization was preformed using La as internal standard. A distinct linear correlation and an excellent coefficient of determination ($R^2 = 0.9988$) can be observed for the Al signal (*cf.* Fig. 2a). The limit of detection (LOD) of the analysis (calculated based on the slope and the standard deviation of the response of the calibration curve) is 0.049 m%, which shows that the selected measurement parameters offer sufficient sensitivity for an accurate analysis of the Al content, even for the lowest dopant levels. In case of Li the coefficient of determination is lower ($R^2 = 0.9628$), however, also here the signal shows a clear correlation (*cf.* Fig. 2b). It is important to notice that in case of Li the covered mass range is very narrow (highest and lowest standard only differ by 17% relatively) and obtaining a suitable calibration therefore difficult. This once more highlights the importance of a high-precision analysis for this material system.

Beside the LA-ICP-OES calibration, Fig. 2 also displays the results of analog LA-ICP-MS measurements for comparative purposes. While the calibration shows similar quality in case of Al (*cf.* Fig. 2c), no significant correlation at all can be observed for the Li signal when ICP-MS is used for the analysis (*cf.* Fig. 2d). This is mostly likely caused by the fact that the measurement of light elements such as Li suffers severely from matrix-induced suppression in the ion beam,[50] limiting the precision of the ICP-MS analysis. The lack of precision in case of LA-ICP-MS confirms that LA-ICP-OES is more reliable for the measurement of Li and is therefore the preferred choice for the analysis of LLZO.

An important aspect for reliable signal quantification is the use of appropriate signal normalization, especially if the used calibration standards potentially show different ablation behavior due to differences in the mechanical properties (ablation rate compact samples *vs.* pressed standards). The most straightforward normalization approach for the analysis of LLZO is the use of La as internal standard, assuming that the same amount of La is present in all standards and samples. This assumption is most likely valid, since La_2O_3 is very heat resistant (melting point > 2300 °C) and occurrence of La loss during the LLZO synthesis is therefore very unlikely. Our experiments confirm this, since we obtain good LA calibrations when we use La for signal normalization (*cf.* Fig. 2). However, assuming a constant La content introduces an additional uncertainty, potentially decreasing the precision of the analysis. Furthermore, it is not possible to determine the full stoichiometry of LLZO samples using that approach, since the La content is not investigated.

To overcome this issues, we applied an adapted version of internal standard-independent calibration strategy presented by Liu *et al.*[48] This approach is based on the consideration that the sum of all metal oxides in LLZO adds up to 100 m% and uses intensities of all measured analytes for signal normalization. Since the mass fractions of all cations (including La) are determined, this calibration strategy enables the calculation of all cation atomic ratios, giving access to the complete stoichiometry of the material.

To determine the accuracy of this quantification strategy, we used a cross-validation approach: in a first step, the stoichiometry (expressed as atomic ratios) of each standard is determined using all other standards for the calibration of the measurement. After that, the obtained values are compared with the corresponding target values (derived from the standard characterization *via* ICP-OES). Fig. 3 shows the results of this cross-validation. In general, excellent agreement between measured and target stoichiometry can be observed. The average deviations for the Al/La, Li/La, and Zr/La atomic ratio are 3.1%, 1.1%, and 0.5%, respectively. Solely the Al/La ratio for the sample with the lowest Al content shows a significantly larger deviation. The reason for this is the low absolute Al concentration in the material, which leads to low signal intensity and therefore large relative measurement uncertainties. This is in agreement with the relatively large error bars for the low-Al standards. Overall, the measurements confirm that the
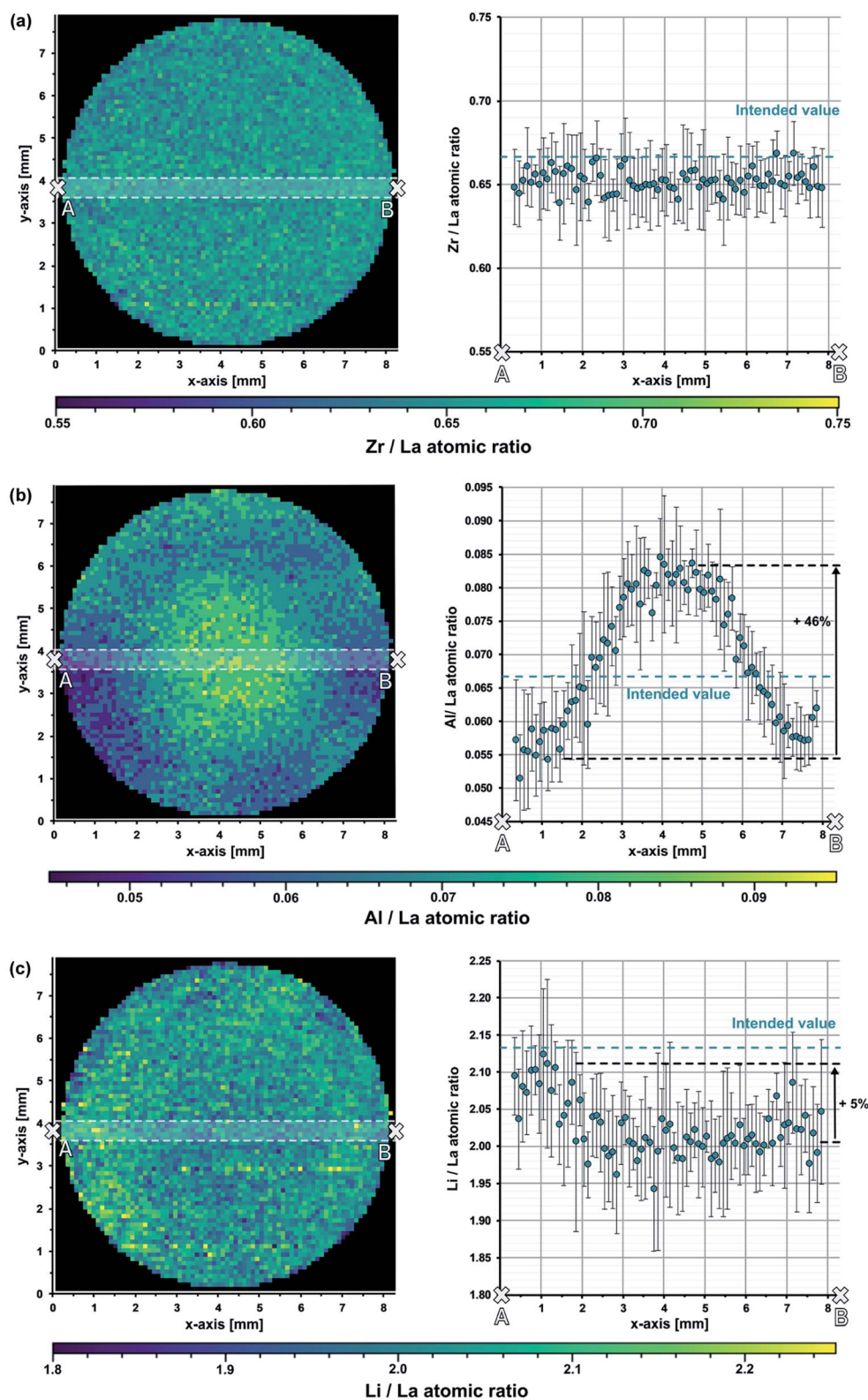
Fig. 4 Quantitative LA-ICP-OES imaging of a LLZO pellet with the nominal composition $Li_{6.4}Al_{0.2}La_3Zr_2O_{12}$. (a) Zr/La, (b) Al/La, and (c) Li/La distribution maps and corresponding atomic ratios along the cross-section from A to B. Each data point in the cross-section plot represents the mean value of five pixels adjacent in the y-direction; the error bars represent the corresponding confidence intervals ($\alpha = 0.10$, $n = 5$). The images show a strong Al-enrichment in the middle of the pellet as well as small but significant variations of the Li content.

internal standard-independent calibration strategy based on 100 m% is reliable for the analysis of LLZO samples.

3.4 Quantitative LLZO imaging

Using the developed quantification strategy, we investigated an Al stabilized LLZO pellet with a nominal composition of $Li_{6.4}Al_{0.2}La_3Zr_2O_{12}$. For that purpose, we performed a 2D distribution imaging experiment covering the whole pellet.

Since the aim of this experiment is to investigate the bulk of the material, we took two measures to avoid influences of surface effects: first, we mechanically removed near surface layers that could be affected by Al-enrichment[38] or other surface-related composition variations. Second, we employed a pre-ablation step directly before the measurement (ablating ca. 2 μm), removing potential surface alterations caused by the grinding process or contact with air (e.g. Li_2CO_3 formation[27]).

The imaging experiment resulted in distribution maps with a lateral resolution of 100 μm in both vertical and horizontal direction. The ablation depth of the analysis was approx. 3 μm. Due to use of the 100 m% normalization strategy, we obtain the mass fractions of all cations (Al, La, Li, and Zr) by the analysis. We converted the mass fractions into the corresponding atomic ratios, which define the stoichiometry of the material.

Fig. 4 shows the obtained distribution images. The maps represent the (locally resolved) sample stoichiometry expressed in form of atomic ratios (Al/La, Li/La, and Zr/La). Significant composition differences between the inner and the outer part of the pellet can be observed. For a better visualization of these variations, the atomic ratios along a selected cross section are plotted next to the corresponding images. To verify that the selected cross-section is representative for the sample, additional cross-sections were investigated, leading to similar results (not shown). As expected, the sample shows a constant Zr/La atomic ratio across the whole pellet (cf. Fig. 4a). Since it is extremely unlikely that the Zr and La content changes in the same ratio, this confirms that Zr as well as La are evenly distributed within the pellet. This is not surprising, since both elements are not prone to evaporation of their oxide, and, moreover, their crystal sites are not affected by Li. Hence, they are most likely not changed by the sintering process. In contrast to that, significant Al and Li variations are observed. The Al/La map shows a strong Al-enrichment in the inner part of the pellet with an increase of Al/La atomic ratio up to 46% compared to the outer part of the sample (cf. Fig. 4b). Considering the fact that Al replaces Li in the LLZO

crystal lattice, the Li distribution image should show an opposing trend. Indeed the Li/La image indicates a higher Li content in the outer part of pellet (cf. Fig. 4c), however, the differences are much smaller and hardly visible in the map. The reason why the variations are much harder to see in case of Li is the fact that LLZO contains a relatively high amount of Li. The changes of the Li-content that are induced by Al-doping are therefore relatively small, making the variations less pronounced. Interestingly, the images show that the Li-content is significantly lower than intended, indicating that more Li than expected was lost during the sintering process.

The obtained distribution images demonstrate the existence of stoichiometry variations within the bulk of LLZO samples. These composition changes are of great relevance since they might affect the electrochemical behavior of LLZO, which is crucial for its application as solid electrolyte material. Possible correlations were investigated in one of our recent studies, where we analyzed several LLZO pellets using the presented method and combined the findings with local conductivity measurements.[51]

3.5 Method validation

In addition to visualizing the analyte distributions, we used the recorded images to determine the mean sample stoichiometry. For that purpose, we averaged the values of all measured pixels. Under the assumption that the pellet does not show composition changes perpendicular to the surface, this represents the average stoichiometry of the analyzed pellet. This assumption is valid since (a) the investigated pellet was very thin (we reduced the thickness of the pellet to about 250 μm, see experimental) and (b) the distribution maps revealed that the stoichiometry changes are on a macroscopic rather than a microscopic scale.

In a further step, we determined the bulk composition of the pellet via conventional ICP-OES analysis. For that purpose, we analyzed the remaining pellet using the same procedure as for the characterization of the standard powders.

In order to validate the accuracy of the LA measurement, we compared the average stoichiometry derived from the distribution images with the bulk composition of the sample determined via ICP-OES. The results of the comparison are summarized in Table 4. The determined values agree very well with relative deviations below 2% for the Al/La, Li/La as well as the Zr/La atomic ratios. This excellent agreement confirms the accuracy of the developed LA-ICP-OES analysis.

Table 4 Comparison of the average sample stoichiometry determined via LA-ICP-OES imaging with the bulk composition determined using conventional ICP-OES analysis. The stated measurement uncertainties of the LA measurement correspond to the double standard deviations of all averaged pixels; the stated measurement uncertainties of the liquid measurement correspond to the confidence intervals of the mean values derived from the measurement of three replicate digestions ($\alpha = 0.10$, $n = 3$). Both methods show excellent agreement

		LA-ICP-OES	ICP-OES (liquid)	Relative deviation
Atomic ratio	Li/La	2.03 ± 0.12	2.05 ± 0.05	−0.9%
	Al/La	0.068 ± 0.016	0.067 ± 0.007	1.7%
	Zr/La	0.65 ± 0.03	0.661 ± 0.006	−1.4%
Formula		$Li_{6.09}Al_{0.20}La_3Zr_{1.96}O_{11.8}$	$Li_{6.15}Al_{0.20}La_3Zr_{1.98}O_{11.9}$	

980 | J. Anal. At. Spectrom., 2020, 35, 972–983

This journal is © The Royal Society of Chemistry 2020

4. Conclusion

We successfully demonstrated the use of LA-ICP-OES for the laterally resolved analysis of the solid electrolyte material LLZO. Reliable signal quantification was achieved by combining the use of in-house prepared and carefully characterized matrixed-matched standards with an internal-standard independent calibration strategy based on 100 m% normalization. The analysis shows a significantly improved precision for the Li determination compared to analog LA-ICP-MS measurements, confirming that OES is better suited for the investigation of this material system.

The recorded distribution images revealed macroscopic composition variations within the bulk of Al-stabilized LLZO samples. Beside strong Al inhomogeneities, also significant variations in the Li content were observed. The stoichiometry variations were most likely caused by the high-temperature treatment during the synthesis, leading to loss of Li_2O and Al diffusion. Moreover, the Li_2O loss depends on the Al content, with less loss for Al-rich samples.

The obtained results demonstrate the importance of spatially resolved sample characterization. Stoichiometry variations might strongly affect the electrochemical behavior of a solid electrolyte material and need to be monitored for that reason. To get a deep understanding of the material properties, combining electrochemical measurements with spatially resolved chemical analysis is necessary.

Conflicts of interest

There are no conflicts to declare.

Acknowledgements

References

1 J. M. Tarascon and M. Armand, Issues and challenges facing rechargeable lithium batteries, *Nature*, 2001, **414**, 359–367.

2 K. Xu, Nonaqueous Liquid Electrolytes for Lithium-Based Rechargeable Batteries, *Chem. Rev.*, 2004, **104**, 4303–4418.

3 K. Takada, Progress and prospective of solid-state lithium batteries, *Acta Mater.*, 2013, **61**, 759–770.

4 P. Knauth, Inorganic solid Li ion conductors, *Solid State Ionics*, 2009, **180**, 911–916.

5 A. D. Robertson, A. R. West and A. G. Ritchie, Review of crystalline lithium-ion conductors suitable for high temperature battery applications, *Solid State Ionics*, 1997, **104**, 1–11.

6 A. Manthiram, X. Yu and S. Wang, Lithium battery chemistries enabled by solid-state electrolytes, *Nat. Rev. Mater.*, 2017, **2**, 294.

7 F. Zheng, M. Kotobuki, S. Song, M. O. Lai and L. Lu, Review on solid electrolytes for all-solid-state lithium-ion batteries, *J. Power Sources*, 2018, **389**, 198–213.

8 Y. Meesala, A. Jena, H. Chang and R. S. Liu, Recent Advancements in Li-Ion Conductors for All-Solid-State Li-Ion Batteries, *ACS Energy Lett.*, 2017, **2**, 2734–2751.

9 X.-B. Cheng, R. Zhang, C.-Z. Zhao and Q. Zhang, Toward Safe Lithium Metal Anode in Rechargeable Batteries: A Review, *Chem. Rev.*, 2017, **117**, 10403–10473.

10 R. Murugan, V. Thangadurai and W. Weppner, Fast lithium ion conduction in garnet-type $Li_7La_3Zr_2O_{12}$, *Angew. Chem., Int. Ed.*, 2007, **46**, 7778–7781.

11 V. Thangadurai, S. Narayanan and D. Pinzaru, Garnet-type solid-state fast Li ion conductors for Li batteries: critical review, *Chem. Soc. Rev.*, 2014, **43**, 4714–4727.

12 V. Thangadurai, D. Pinzaru, S. Narayanan and A. K. Baral, Fast Solid-State Li Ion Conducting Garnet-Type Structure Metal Oxides for Energy Storage, *J. Phys. Chem. Lett.*, 2015, **6**, 292–299.

13 Q. Liu, Z. Geng, C. Han, Y. Fu, S. Li, Y.-b. He, F. Kang and B. Li, Challenges and perspectives of garnet solid electrolytes for all solid-state lithium batteries, *J. Power Sources*, 2018, **389**, 120–134.

14 J. Awaka, N. Kijima, H. Hayakawa and J. Akimoto, Synthesis and structure analysis of tetragonal $Li_7La_3Zr_2O_{12}$ with the garnet-related type structure, *J. Solid State Chem.*, 2009, **182**, 2046–2052.

15 J. Wolfenstine, E. Rangasamy, J. L. Allen and J. Sakamoto, High conductivity of dense tetragonal $Li_7La_3Zr_2O_{12}$, *J. Power Sources*, 2012, **208**, 193–196.

16 C. A. Geiger, E. Alekseev, B. Lazic, M. Fisch, T. Armbruster, R. Langner, M. Fechtelkord, N. Kim, T. Pettke and W. Weppner, Crystal chemistry and stability of "$Li_7La_3Zr_2O_{12}$" garnet, *Inorg. Chem.*, 2011, **50**, 1089–1097.

17 H. Buschmann, J. Dölle, S. Berendts, A. Kuhn, P. Bottke, M. Wilkening, P. Heitjans, A. Senyshyn, H. Ehrenberg, A. Lotnyk, V. Duppel, L. Kienle and J. Janek, Structure and dynamics of the fast lithium ion conductor "$Li_7La_3Zr_2O_{12}$", *Phys. Chem. Chem. Phys.*, 2011, **13**, 19378–19392.

18 M. Kotobuki, K. Kanamura, Y. Sato and T. Yoshida, Fabrication of all-solid-state lithium battery with lithium metal anode using Al_2O_3-added $Li_7La_3Zr_2O_{12}$ solid electrolyte, *J. Power Sources*, 2011, **196**, 7750–7754.

19 A. Wachter-Welzl, J. Kirowitz, R. Wagner, S. Smetaczek, G. C. Brunauer, M. Bonta, D. Rettenwander, S. Taibl, A. Limbeck, G. Amthauer and J. Fleig, The origin of conductivity variations in Al-stabilized $Li_7La_3Zr_2O_{12}$ ceramics, *Solid State Ionics*, 2018, **319**, 203–208.

20 A. Wachter-Welzl, R. Wagner, D. Rettenwander, S. Taibl, G. Amthauer and J. Fleig, Microelectrodes for local conductivity and degradation measurements on Al stabilized $Li_7La_3Zr_2O_{12}$ garnets, *J. Electroceram.*, 2017, **38**, 176–181.

21 L. Cheng, J. S. Park, H. Hou, V. Zorba, G. Chen, T. Richardson, J. Cabana, R. Russo and M. Doeff, Effect of microstructure and surface impurity segregation on the electrical and electrochemical properties of dense Al-substituted $Li_7La_3Zr_2O_{12}$, *J. Mater. Chem. A*, 2014, **2**, 172–181.

22 C.-L. Tsai, E. Dashjav, E.-M. Hammer, M. Finsterbusch, F. Tietz, S. Uhlenbruck and H. P. Buchkremer, High

This journal is © The Royal Society of Chemistry 2020

J. Anal. At. Spectrom., 2020, **35**, 972–983 | 981

conductivity of mixed phase Al-substituted $Li_7La_3Zr_2O_{12}$, *J. Electroceram.*, 2015, **35**, 25–32.

23 H. El-Shinawi, G. W. Paterson, D. A. MacLaren, E. J. Cussen and S. A. Corr, Low-temperature densification of Al-doped $Li_7La_3Zr_2O_{12}$, *J. Mater. Chem. A*, 2017, **5**, 319–329.

24 X. X. Pan, J. X. Wang, X. H. Chang, Y. D. Li and W. B. Guan, A novel solid-liquid route for synthesizing cubic garnet Al-substituted $Li_7La_3Zr_2O_{12}$, *Solid State Ionics*, 2018, **317**, 1–6.

25 J. Wolfenstine, J. Sakamoto and J. L. Allen, Electron microscopy characterization of hot-pressed Al substituted $Li_7La_3Zr_2O_{12}$, *J. Mater. Sci.*, 2012, **47**, 4428–4431.

26 K. H. Kim, T. Hirayama, C. A. J. Fisher, K. Yamamoto, T. Sato, K. Tanabe, S. Kumazaki, Y. Iriyama and Z. Ogumi, Characterization of grain-boundary phases in $Li_7La_3Zr_2O_{12}$ solid electrolytes, *Mater. Charact.*, 2014, **91**, 101–106.

27 L. Cheng, E. J. Crumlin, W. Chen, R. Qiao, H. Hou, S. Franz Lux, V. Zorba, R. Russo, R. Kostecki, Z. Liu, K. Persson, W. Yang, J. Cabana, T. Richardson, G. Chen and M. Doeff, The origin of high electrolyte-electrode interfacial resistances in lithium cells containing garnet type solid electrolytes, *Phys. Chem. Chem. Phys.*, 2014, **16**, 18294–18300.

28 L. Cheng, C. H. Wu, A. Jarry, W. Chen, Y. Ye, J. Zhu, R. Kostecki, K. Persson, J. Guo, M. Salmeron, G. Chen and M. Doeff, Interrelationships among Grain Size, Surface Composition, Air Stability, and Interfacial Resistance of Al-Substituted $Li_7La_3Zr_2O_{12}$ Solid Electrolytes, *ACS Appl. Mater. Interfaces*, 2015, **7**, 17649–17655.

29 W. Xia, B. Xu, H. Duan, Y. Guo, H. Kang, H. Li and H. Liu, Ionic Conductivity and Air Stability of Al-Doped $Li_7La_3Zr_2O_{12}$ Sintered in Alumina and Pt Crucibles, *ACS Appl. Mater. Interfaces*, 2016, **8**, 5335–5342.

30 M. Zarabian, M. Bartolini, P. Pereira-Almao and V. Thangadurai, X-ray Photoelectron Spectroscopy and AC Impedance Spectroscopy Studies of Li-La-Zr-O Solid Electrolyte Thin Film/$LiCoO_2$ Cathode Interface for All-Solid-State Li Batteries, *J. Electrochem. Soc.*, 2017, **164**, A1133.

31 A. Sharafi, S. Yu, M. Naguib, M. Lee, C. Ma, H. M. Meyer, J. Nanda, M. Chi, D. J. Siegel and J. Sakamoto, Impact of air exposure and surface chemistry on $Li–Li_7La_3Zr_2O_{12}$ interfacial resistance, *J. Mater. Chem. A*, 2017, **5**, 13475–13487.

32 S. Uhlenbruck, C. Dellen, S. Möller, S. Lobe, C.-L. Tsai, M. Finsterbusch, M. Bram and O. Guillon, Reactions of garnet-based solid-state lithium electrolytes with water — A depth-resolved study, *Solid State Ionics*, 2018, **320**, 259–265.

33 F. M. Pesci, R. H. Brugge, A. K. O. Hekselman, A. Cavallaro, R. J. Chater and A. Aguadero, Elucidating the role of dopants in the critical current density for dendrite formation in garnet electrolytes, *J. Mater. Chem. A*, 2018, **6**, 19817–19827.

34 R. H. Brugge, A. K. O. Hekselman, A. Cavallaro, F. M. Pesci, R. J. Chater, J. A. Kilner and A. Aguadero, Garnet Electrolytes for Solid State Batteries, *Chem. Mater.*, 2018, **30**, 3704–3713.

35 R. H. Brugge, J. A. Kilner and A. Aguadero, Germanium as a donor dopant in garnet electrolytes, *Solid State Ionics*, 2019, **337**, 154–160.

36 L. Cheng, H. Hou, S. Lux, R. Kostecki, R. Davis, V. Zorba, A. Mehta and M. Doeff, Enhanced lithium ion transport in garnet-type solid state electrolytes, *J. Electroceram.*, 2017, **38**, 168–175.

37 D. Rettenwander, R. Wagner, A. Reyer, M. Bonta, L. Cheng, M. M. Doeff, A. Limbeck, M. Wilkening and G. Amthauer, Interface Instability of Fe-Stabilized $Li_7La_3Zr_2O_{12}$ versus Li Metal, *J. Phys. Chem. C*, 2018, **122**, 3780–3785.

38 H. Hou, L. Cheng, T. Richardson, G. Chen, M. Doeff, R. Zheng, R. Russo and V. Zorba, Three-dimensional elemental imaging of Li-ion solid-state electrolytes using fs-laser induced breakdown spectroscopy (LIBS), *J. Anal. At. Spectrom.*, 2015, **30**, 2295–2302.

39 A. Limbeck, M. Bonta and W. Nischkauer, Improvements in the direct analysis of advanced materials using ICP-based measurement techniques, *J. Anal. At. Spectrom.*, 2017, **32**, 212–232.

40 J. S. Becker, Applications of inductively coupled plasma mass spectrometry and laser ablation inductively coupled plasma mass spectrometry in materials science, *Spectrochim. Acta, Part B*, 2002, **57**, 1805–1820.

41 M. Kalapsazova, R. Stoyanova, E. Zhecheva, G. Tyuliev and D. Nihtianova, Sodium deficient nickel–manganese oxides as intercalation electrodes in lithium ion batteries, *J. Mater. Chem. A*, 2014, **2**, 19383–19395.

42 T. Schwieters, M. Evertz, M. Mense, M. Winter and S. Nowak, Lithium loss in the solid electrolyte interphase: Lithium quantification of aged lithium ion battery graphite electrodes by means of laser ablation inductively coupled plasma mass spectrometry and inductively coupled plasma optical emission spectroscopy, *J. Power Sources*, 2017, **356**, 47–55.

43 T. Schwieters, M. Evertz, A. Fengler, M. Börner, T. Dagger, Y. Stenzel, P. Harte, M. Winter and S. Nowak, Visualizing elemental deposition patterns on carbonaceous anodes from lithium ion batteries: A laser ablation-inductively coupled plasma-mass spectrometry study on factors influencing the deposition of lithium, nickel, manganese and cobalt after dissolution and migration from the $Li_1[Ni_{1/3}Mn_{1/3}Co_{1/3}]O_2$ and $LiMn_{1.5}Ni_{0.5}O_4$ cathode, *J. Power Sources*, 2018, **380**, 194–201.

44 P. Harte, M. Evertz, T. Schwieters, M. Diehl, M. Winter and S. Nowak, Adaptation and improvement of an elemental mapping method for lithium ion battery electrodes and separators by means of laser ablation-inductively coupled plasma-mass spectrometry, *Anal. Bioanal. Chem.*, 2019, **411**, 581–589.

45 T. Dagger, J. Kasnatscheew, B. Vortmann-Westhoven, T. Schwieters, S. Nowak, M. Winter and F. M. Schappacher, Performance tuning of lithium ion battery cells with area-oversized graphite based negative electrodes, *J. Power Sources*, 2018, **396**, 519–526.

46 A. Limbeck, P. Galler, M. Bonta, G. Bauer, W. Nischkauer and F. Vanhaecke, Recent advances in quantitative LA-ICP-MS analysis: challenges and solutions in the life sciences and environmental chemistry, *Anal. Bioanal. Chem.*, 2015, **407**, 6593–6617.

982 | *J. Anal. At. Spectrom.*, 2020, **35**, 972–983

This journal is © The Royal Society of Chemistry 2020

47 R. Wagner, G. J. Redhammer, D. Rettenwander, A. Senyshyn, W. Schmidt, M. Wilkening and G. Amthauer, Crystal Structure of Garnet-Related Li-Ion Conductor $Li_{7-3x}Ga_xLa_3Zr_2O_{12}$: Fast Li-Ion Conduction Caused by a Different Cubic Modification?, *Chem. Mater.*, 2016, **28**, 1861–1871.

48 Y. Liu, Z. Hu, S. Gao, D. Günther, J. Xu, C. Gao and H. Chen, In situ analysis of major and trace elements of anhydrous minerals by LA-ICP-MS without applying an internal standard, *Chem. Geol.*, 2008, **257**, 34–43.

49 J. Awaka, A. Takashima, K. Kataoka, N. Kijima, Y. Idemoto and J. Akimoto, Crystal Structure of Fast Lithium-ion-conducting Cubic $Li_7La_3Zr_2O_{12}$, *Chem. Lett.*, 2011, **40**, 60–62.

50 E. H. Evans and J. J. Giglio, Interferences in inductively coupled plasma mass spectrometry. A review, *J. Anal. At. Spectrom.*, 1993, **8**, 1.

51 S. Smetaczek, A. Wachter-Welzl, R. Wagner, D. Rettenwander, G. Amthauer, L. Andrejs, S. Taibl, A. Limbeck and J. Fleig, Local Li-ion conductivity changes within Al stabilized $Li_7La_3Zr_2O_{12}$ and their relationship to three-dimensional variations of the bulk composition, *J. Mater. Chem. A*, 2019, **7**, 6818–6831.

This journal is © The Royal Society of Chemistry 2020

J. Anal. At. Spectrom., 2020, **35**, 972–983 | **983**